# Surface Integrity of Ni-Rich NiTi Shape Memory Alloy at Optimized Level of Wire Electric Discharge Machining Parameters

**Himanshu Bisaria** and **Pragya Shandilya**

The concern of this experimental work is to study the surface integrity aspects such as surface morphology, three-dimensional surface topography, recast layer, phase analysis, and micro-hardness for $Ni_{55.95}Ti_{44.05}$ shape memory alloy at the optimized level of wire electric discharge machining parameters. A mathematical model was developed for surface roughness and material removal rate considering servo voltage, pulse on time, wire tension, wire feed rate, and pulse off time using response surface methodology technique. In order to obtain the optimized parameters, multi-objective optimization technique grey relation analysis was utilized. The adequacy of the developed model was also checked by analysis of variance. At optimal parameters setting, i.e., pulse on time 123 µs, pulse off time 58 µs, servo voltage 50 V, wire tension 3 N, and wire feed rate 5 m/min, maximum material removal rate ($8.223$ $mm^3$/min) and minimum surface roughness (1.93 µm) were achieved. Surface characteristics of machined surface divulge the presence of discharge craters, debris, molten droplets, micro-voids, spherical nodules, and cracks. A recast layer of thickness 19 µm with approximately 21% of foreign elements was deposited on the machined surface at optimized parameters, whereas the micro-hardness of the outer machined surface was found to be increased approximately 1.98 times as compared to micro-hardness of bulk material. X-ray diffraction analysis shows the presence of the following compounds on the machined surface NiTi, $Ni_4Ti_3$, $Ti_4O_3$, $Cu_5Zn_8$, $Ni(TiO_3)$, and NiZn.

**List of Symbols**

| | |
|---|---|
| $T_{ON}$ | Pulse on time (µs) |
| $T_{OFF}$ | Pulse off time (µs) |
| $W_g$ | Spark gap |
| $d$ | Wire diameter |

**Abbreviations**

| | |
|---|---|
| WEDM | Wire electric discharge machining |
| SMA | Shape memory alloy |
| SV | Servo voltage (V) |
| WT | Wire tension (N) |
| WF | Wire feed rate (m/min) |
| MRR | Material removal rate ($mm^3$/min) |
| $R_a$ | Surface roughness (µm) |
| RSM | Response surface methodology |
| CCD | Central composite design |
| SEM | Scanning electron microscope |
| EDS | Energy-dispersive spectroscopy |
| XRD | x-ray diffraction |
| GRA | Grey relation analysis |
| GRG | Grey relation coefficient |
| GRC | Grey relation grade |
| ANOVA | Analysis of variance |
| SS | Sum of square |
| MS | Mean square |
| DOF | Degree of freedom |
| CI | Confidence interval |

## 1. Introduction

A wide spectrum of NiTi SMAs' unique properties stimulates the interest of its usage in many sectors such as aerospace, biomedical, robotics, and other important domains because of their exceptional properties (Ref 1-5). In the past few decades, NiTi SMAs undergo considerable modifications in their phenomenal properties like shape memory effect, high wear and corrosion resistant, superelasticity and high specific strength. The same properties that impart uniqueness are also responsible for poor machinability in NiTi SMAs (Ref 6-8). A great proportion of SMA product market is occupied by Ni-rich SMAs (Ref 9). Owing to the poor machinability with conventional methods, it is difficult to maintain simultaneously low surface roughness, high MRR, and high dimensional accuracy (Ref 10, 11). Therefore, these issues must be dealt with extra care; to control these responses, the advanced machining processes must be exploited for effective and profitable machining of NiTi SMAs. However, unconventional machining processes, namely laser beam machining, chemical and elec-

**Himanshu Bisaria** and **Pragya Shandilya**, Mechanical Engineering Department, Motilal Nehru National Institute of Technology Allahabad, Allahabad 211004, India. Contact e-mail: himanshubisaria20@gmail.com.

trochemical machining, abrasive waterjet machining, and electric discharge machining, have their own limitations like burr formation, low surface finish, heat-affected zone, and surface reactions. Among all these advanced machining processes, WEDM has comparatively better suitability for cutting hard and conductive alloys which are difficult to cut by conventional machining processes (Ref 12, 13). In WEDM process, a thin conductive traveling wire is used as electrode and material is removed by a series of rapidly repeated sparks between the workpiece and wire, separated by a dielectric fluid and subjected to electric voltage (Ref 14-16). It can machine any electrically conductive material regardless of the hardness and complex geometries (Ref 17).

Few researchers have attempted the machining of NiTi SMAs by WEDM. Bisaria and Shandilya (Ref 3, 5) performed a parametric study for Ni-rich NiTi SMA during WEDM using one factor at a time approach. It was found that surface integrity aspects (recast layer, surface morphology, micro-hardness, phase analysis, etc.) of the machined surface were predominantly influenced by pulse on time, spark gap voltage, and pulse off time, whereas wire feed rate and wire tension were related to the accuracy, precision, and economics of machining. Hsieh et al. (Ref 12) examined the machining characteristics of NiTi-based ternary SMA in WEDM and concluded that longer pulse duration degraded the surface quality and increased the recast layer thickness. Manjaiah et al. (Ref 18) have explored the machinability of $Ti_{50}Ni_{40}Cu_{10}$ and $Ti_{50}Ni_{30}Cu_{20}$ SMA in WEDM using full factorial design (FFD) approach and concluded that MRR and surface roughness increased with an increase in pulse on time and the decrease in pulse off time and servo voltage. New phases were detected on the machined surface because of the chemical reaction among wire electrode, dielectric, and machined surface at elevated temperature. Liu et al. (Ref 19) examined the properties, composition, and crystallography of white layer for SE508 Nitinol (50.8 at.% Ni-49.2 at.% Ti) in WEDM. A crystalline-structured white layer formed on the machined surface comprises the small number of foreign elements (copper and zinc) from brass wire electrode. The nano-hardness of the white layer was found to be increased compared to the bulk hardness of material due to oxide hardening. For multi-response optimization in WEDM process, researchers have effectively utilized GRA technique. Rajyalakshmi and Ramaiah (Ref 20) optimized the WEDM process parameters for Inconel 825 alloy using Taguchi and GRA. At the optimal set of parameters (using GRA), MRR was increased by 6.04%, whereas surface roughness and spark gap were reduced by 14.29 and 15.384%, respectively, which endorsed the capability of the optimization process. Saha and Mondal (Ref 21) experimentally studied the WEDM process for nano-structured hardfacing material and developed a mathematical model using RSM. Confirmatory experiments validating the Taguchi coupled with principal component analysis (PCA) enhanced the machining performance (MRR and surface roughness) and optimized WEDM process parameters. Majumder et al. (Ref 22) developed RSM model for cutting time and surface roughness of Inconel 800 in WEDM process and optimized the parameters using GRA technique. It was concluded that the predicted values by the developed model were closed to experimental values.

After a detailed scrutiny of the literature, it has been concluded that the domain of previous research works was directed to the effect of WEDM parameters on performance characteristics of NiTi SMAs. Some attempt has been made

keeping in view of the optimization, but the study on surface integrity aspects after optimization for Ni-rich NiTi SMA has been seldom reported which is novel and interesting aspects of this experimental study. The present study focuses on the modeling and multi-objective optimization of WEDM parameters for $Ni_{55.95}Ti_{44.05}$ SMA, considering MRR and $R_a$ as response parameters and $T_{ON}$, $T_{OFF}$, SV, WF, and WT as variable parameters. CCD of RSM technique has been adopted for developing a mathematical model for MRR and $R_a$. For studying surface integrity aspects, GRA approach was used to find out optimized process parameters at which maximum MRR and minimum $R_a$ can be achieved. Phase analysis, micro-hardness, surface characteristics, and recast layer have been studied under surface integrity aspects by using XRD, Vickers micro-hardness tester, SEM, optical profilometer, and EDS technique, respectively.

## 2. Materials and Methodology

### 2.1 Material

For the experimental studies, a square plate of $Ni_{55.95}Ti_{44.05}$ (55.95-wt.% Ni and 44.05-wt.% Ti) SMA with a density of 6.7 g/cm$^3$ and dimensions 165 mm × 165 mm × 6 mm has been procured. The elemental composition (wt.%) of $Ni_{55.95}Ti_{44.05}$ SMA was detected by EDS test conducted at 20 kV accelerating voltage. The phenomena of shape recovery ability by the application of stress and heat are associated with martensitic phase transformation between austenite and martensite phase. The austenite start, austenite finish, martensite start, and martensite finish temperatures were detected 304.6, 329.34, 283.48, and 258.65 K, respectively, by differential scanning calorimeter test (Ref 3, 5).

### 2.2 Design of Experiments

The range and levels of WEDM parameters have been decided on the basis of preliminary experiments by using one parameter at a time technique. WEDM parameters such as $T_{ON}$, SV, WT, $T_{OFF}$, and WF have been considered as variable to examine their effects on $R_a$ and MRR for $Ni_{55.95}Ti_{44.05}$ SMA. The range and levels of variable parameters are represented in Table 1. A thin brass wire of diameter 0.25 mm as an electrode has been selected in this study. The pulse peak current, pressure of the dielectric fluid (deionized water), and dielectric conductivity were fixed at 12 A, 1 kg/cm$^2$, and ± 20-24 μs/m, respectively. A CCD technique of RSM has been employed to design the experiments. RSM is a collection of statistical and mathematical techniques in which desired response is affected by multi-variables. RSM can be utilized for modeling and analysis of engineering problems (Ref 23). During this process, the influence of all the process parameters on responses is collectively analyzed, instead of one factor at a time analysis.

The relation between response $z$ and $i$ variable factors $y_1$, $y_2$, $y_3$, $y_4$.... $y_i$ is represented according to Eq 1.

$$z = \Phi(y_1, y_2, y_3 \ldots y_i) + \zeta \qquad (\text{Eq 1})$$

where $\Phi$ is response function and $\zeta$ represents noise or error. Let us consider $f(z)$ is desirable response function and $x_i$, $x_j$, ...$x_n$ are the independent variable parameters. The quadratic model for $f(z)$ can be written as follows:

**Table 1 WEDM variable parameters for $Ni_{55.95}Ti_{44.05}$ SMA**

| Parameters | Unit | Symbol | Range (available on machine) | Range (after pilot test) | Levels | | | | |
|---|---|---|---|---|---|---|---|---|---|
| | | | | | − 2 | − 1 | 0 | 1 | 2 |
| $T_{ON}$ | μs | A | 105-130 | 115-123 | 115 | 117 | 119 | 121 | 123 |
| $T_{OFF}$ | μs | B | 45-63 | 52-60 | 52 | 54 | 56 | 58 | 60 |
| SV | V | C | 5-75 | 35-55 | 35 | 40 | 45 | 50 | 55 |
| WT | N | D | 1-10 | 2-6 | 2 | 3 | 4 | 5 | 6 |
| WF | m/min | E | 1-15 | 2-6 | 2 | 3 | 4 | 5 | 6 |

$$f(z) = \alpha_o + \sum_{i=1}^{n} \alpha_i x_i + \sum_{i=1}^{n} \alpha_{ii} x_i^2 + \sum_{i<j} \alpha_{ij} x_i x_j \qquad (Eq\ 2)$$

where $\alpha_o$, $\alpha_i$, $\alpha_j$, and $\alpha_{ij}$ are intercept term, linear coefficient, quadratic coefficient, and interaction term, respectively. For this study $T_{ON}$, $T_{OFF}$, SV, WF, and WT are variable parameters and MRR and $R_a$ are desirable response parameters.

CCD is a well-known technique for designing five-factor and five-level type problems owing to the flexibility and minimum error (Ref 23). For constructing second-order model in CCD, each parameter is varied at five levels (− 2, − 1, 0, 1, and 2). According to central composite rotatable design, with five process parameters at a full fraction, a total of 50 experiments have been performed for modeling and analysis as per given in Eq 3.

$$No.\ experimental\ runs\ = 2^f + 2 \times f + N_c$$
$$= 2^5 + 2 \times 5 + 8 = 50 \qquad (Eq\ 3)$$

where $f$ is factors and $N_c$ is center points. This five-factor and five-level design includes 32 ($2^5$) full factorial points, 10 axial points ($\alpha = \pm 2$), and 8 center points (zero levels). The design matrix for experiments and responses is shown in Table 2.

### 2.3 Experimental Procedure

The machining was conducted on computer numerical control, four axes, Ultracut-843, WEDM. The effect of WEDM process parameters, namely, $T_{ON}$, $T_{OFF}$, SV, WT, and WF, on MRR and $R_a$ has been studied. The specimens with the dimension of 10 mm × 10 mm × 6 mm were machined. The digital stopwatch was used for calculating machining time. Equation 4 was utilized to calculate MRR (Ref 24).

$$MRR\ (mm^3/min)\ =\ cutting\ speed\ (mm/min)$$
$$\times\ thickness\ of\ sample\ (mm)$$
$$\times\ width\ of\ cut\ (mm) \qquad (Eq\ 4)$$

where thickness of sample is 6 mm; width of cut = $2W_g + d$; $W_g$ is spark gap (0.02 mm); and $d$ is wire diameter (0.25 mm).

$R_a$ (average surface roughness) of the machined surface has been measured by "Mitutoyo SJ-410" surface roughness tester. The surface roughness for the individual sample was recorded at five distinct points, and the average was considered as a response parameter. The stylus speed and cutoff length were 0.1 mm/s and 0.8 mm, respectively, used to evaluate the length of 4 mm. PANalytical X'PERT x-ray analyzer was utilized to analyze the phase change of machined surface using Cu-Kα radiation at room temperature. The power was 45 kV × 40 mA, and the scanning rate of $2\theta$ (5°-100°) was 3° $min^{-1}$. JEOL

JSM-6010LA SEM attached with EDS facility was used for the morphological analysis of machined surface. The thickness of the recast layer was measured by the analysis of a cross-sectional SEM image of the machined surface with the help of ImageJ software by using Eq 5 (Ref. 7).

$$Recast\ layer\ thickness\ = \frac{Area\ of\ recast\ layer\ (\mu m^2)}{Length\ of\ recast\ layer\ (\mu m)}$$
$$(Eq\ 5)$$

Bruker contour GTK optical profiler was exploited for analyzing three-dimensional surface topography. For the analysis of three-dimensional surface topography, the sample area was $240 \times 180\ \mu m^2$. The three-dimensional surface topography can be also utilized for the measurement of the height of the protrusion and the depth of depression on the machined surface.

CSM micro-hardness tester having square-shaped pyramidal indenter of the diamond at the load of 250 mN and dwell time of 15 s has been utilized to measure micro-hardness. The micro-hardness was measured by Eq 6 (Ref 5).

$$Vicker\ hardness\ (Hv)\ = \frac{2P Sin\frac{136°}{2}}{D^2} \qquad (Eq\ 6)$$

where $P$ is applied load (N) and $D$ (mm) is the average of two diagonal indenters having an angle of 136°.

## 3. Results and Discussion

### 3.1 ANOVA for Material Removal Rate

The experimental results (given in Table 2) were analyzed by using Design Expert 9.0.5 software. ANOVA results for MRR are summarized in Table 3. As per obtained fit summary from the analysis, it can be noticed that the quadratic model developed for MRR is statistically significant. In order to remove nonsignificant terms in the developed model, the backward elimination with a 95% CI is used. The F value of the model is 52.42 which validates that the developed model is significant. There is only 0.01% possibility that an $F$ value this large could occur due to noise. The probability value (Prob > $F$ or $p$ value) < 0.05 designates the significance of model terms. As per ANOVA results, for MRR, the parameters $T_{ON}$, $T_{OFF}$, SV, square of $T_{ON}$, square of $T_{OFF}$, square of SV and interaction of SV and $T_{OFF}$ were the significant factors, whereas WF and WT were insignificant. The $F$ value of lack of fit is 2.54 which infers that there is a 10.39% possibility that an "$F$ value of lack of fit" of this large could occur due to noise. Determination coefficient ($R^2$) value is 0.9658 which indicates

**Table 2 Experimental design and observed results**

| Standard run | $T_{ON}$, μs | $T_{OFF}$, μs | SV, V | WT, N | WF, m/min | MRR, mm³/min | $R_a$, μm |
|---|---|---|---|---|---|---|---|
| 1 | 117 | 54 | 40 | 3 | 3 | 6.755 | 2.13 |
| 2 | 121 | 54 | 40 | 3 | 3 | 7.024 | 2.18 |
| 3 | 117 | 58 | 40 | 3 | 3 | 6.307 | 1.84 |
| 4 | 121 | 58 | 40 | 3 | 3 | 6.935 | 1.86 |
| 5 | 117 | 54 | 50 | 3 | 3 | 6.618 | 1.91 |
| 6 | 121 | 54 | 50 | 3 | 3 | 7.023 | 2.22 |
| 7 | 117 | 58 | 50 | 3 | 3 | 5.554 | 1.61 |
| 8 | 121 | 58 | 50 | 3 | 3 | 5.533 | 1.92 |
| 9 | 117 | 54 | 40 | 5 | 3 | 6.629 | 2.1 |
| 10 | 121 | 54 | 40 | 5 | 3 | 6.985 | 2.24 |
| 11 | 117 | 58 | 40 | 5 | 3 | 6.280 | 1.84 |
| 12 | 121 | 58 | 40 | 5 | 3 | 6.914 | 1.87 |
| 13 | 117 | 54 | 50 | 5 | 3 | 6.854 | 1.85 |
| 14 | 121 | 54 | 50 | 5 | 3 | 7.353 | 2.23 |
| 15 | 117 | 58 | 50 | 5 | 3 | 4.743 | 1.63 |
| 16 | 121 | 58 | 50 | 5 | 3 | 5.179 | 1.98 |
| 17 | 117 | 54 | 40 | 3 | 5 | 6.283 | 2.13 |
| 18 | 121 | 54 | 40 | 3 | 5 | 7.635 | 2.23 |
| 19 | 117 | 58 | 40 | 3 | 5 | 6.296 | 1.84 |
| 20 | 121 | 58 | 40 | 3 | 5 | 7.293 | 1.86 |
| 21 | 117 | 54 | 50 | 3 | 5 | 6.147 | 1.81 |
| 22 | 121 | 54 | 50 | 3 | 5 | 7.317 | 2.22 |
| 23 | 117 | 58 | 50 | 3 | 5 | 5.171 | 1.51 |
| 24 | 121 | 58 | 50 | 3 | 5 | 5.428 | 1.83 |
| 25 | 117 | 54 | 40 | 5 | 5 | 5.713 | 2.15 |
| 26 | 121 | 54 | 40 | 5 | 5 | 7.420 | 2.26 |
| 27 | 117 | 58 | 40 | 5 | 5 | 5.787 | 1.77 |
| 28 | 121 | 58 | 40 | 5 | 5 | 7.341 | 1.98 |
| 29 | 117 | 54 | 50 | 5 | 5 | 6.529 | 1.93 |
| 30 | 121 | 54 | 50 | 5 | 5 | 7.917 | 2.12 |
| 31 | 117 | 58 | 50 | 5 | 5 | 4.660 | 1.52 |
| 32 | 121 | 58 | 50 | 5 | 5 | 6.294 | 1.94 |
| 33 | 115 | 56 | 45 | 4 | 4 | 6.701 | 1.73 |
| 34 | 123 | 56 | 45 | 4 | 4 | 8.554 | 2.12 |
| 35 | 119 | 52 | 45 | 4 | 4 | 6.169 | 2.35 |
| 36 | 119 | 60 | 45 | 4 | 4 | 4.386 | 1.78 |
| 37 | 119 | 56 | 35 | 4 | 4 | 5.569 | 2.21 |
| 38 | 119 | 56 | 55 | 4 | 4 | 4.194 | 2.01 |
| 39 | 119 | 56 | 45 | 2 | 4 | 5.722 | 1.99 |
| 40 | 119 | 56 | 45 | 6 | 4 | 5.613 | 1.99 |
| 41 | 119 | 56 | 45 | 4 | 2 | 5.755 | 2.05 |
| 42 | 119 | 56 | 45 | 4 | 6 | 5.783 | 2 |
| 43 | 119 | 56 | 45 | 4 | 4 | 4.620 | 1.99 |
| 44 | 119 | 56 | 45 | 4 | 4 | 4.994 | 2.12 |
| 45 | 119 | 56 | 45 | 4 | 4 | 4.807 | 1.98 |
| 46 | 119 | 56 | 45 | 4 | 4 | 4.666 | 2.08 |
| 47 | 119 | 56 | 45 | 4 | 4 | 4.476 | 2.07 |
| 48 | 119 | 56 | 45 | 4 | 4 | 4.777 | 2.08 |
| 49 | 119 | 56 | 45 | 4 | 4 | 4.854 | 2.07 |
| 50 | 119 | 56 | 45 | 4 | 4 | 4.937 | 2.06 |

that this developed model is capable to explain 96.58% variation and rest 3.42% variations may not be explained. The predicted $R^2$ (0.8832) is in realistic agreement with the adjusted-$R^2$ (0.9423) since the difference is < 0.2. Adequate precision measures the ratio of signal to noise (i.e., ratio of significant factors to nonsignificant factors); the value should be greater than 4 for a model to be adequate. The value of adequate precision is 25.60 (i.e., large signal-to-noise ratio) which also validates that the developed model is significant. Square of $T_{ON}$ has the highest percentage contribution followed by $T_{OFF}$, $T_{ON}$, and SV.

The mathematical relationship between MRR and variable parameters in coded form is given in Eq 7. The equation in coded form can be used to predict the value of MRR at a given level of variable parameters. The high levels of the parameters are assigned + 1 code, and the low-level factors are coded as − 1. This coded equation is useful for finding the relative influence of the factors by comparing the coefficients of factors. Equation 8 depicts the mathematical relationship in actual factors which can also be used to make predictions of MRR at a given level of each factor; however, the levels should be specified in the original units for each factor. This developed

**Table 3  ANOVA table for material removal rate**

| Source | SS | DOF | MS | $F$ value | $p$ value Prob > $F$ | Remarks | Percentage contribution |
|---|---|---|---|---|---|---|---|
| Model | 52.42 | 20 | 2.62 | 40.99 | < 0.0001 | Significant | … |
| A | 7.20 | 1 | 7.20 | 112.60 | < 0.0001 | Significant | 15.60 |
| B | 8.15 | 1 | 8.15 | 127.39 | < 0.0001 | Significant | 17.66 |
| C | 3.62 | 1 | 3.62 | 56.54 | < 0.0001 | Significant | 7.84 |
| BC | 4.43 | 1 | 4.43 | 69.28 | < 0.0001 | Significant | 9.59 |
| $A^2$ | 19.44 | 1 | 19.44 | 304.02 | < 0.0001 | Significant | 42.12 |
| $B^2$ | 1.18 | 1 | 1.18 | 18.43 | 0.0002 | Significant | 2.55 |
| $C^2$ | 0.28 | 1 | 0.28 | 4.32 | 0.0467 | Significant | 0.61 |
| Residual | 1.85 | 29 | 0.064 | | | | |
| Lack of fit | 1.65 | 22 | 0.075 | 2.54 | 0.1039 | Not significant | |
| Pure error | 0.21 | 7 | 0.029 | | | | $R^2$ = 0.9658 |
| Corrected total | 46.15 | 49 | | | | | Adjusted-$R^2$ = 0.9423 |
| | | | | | | | Predicted $R^2$ = 0.8832 |
| | | | | | | | Adequate precision = 25.60 |

equation is not sufficient to identify the relative influence of individual factor since the coefficients are scaled to accommodate the units of each factor and the intercept is not at the center of the design space.

Figure 1(a) and (b) shows the variation of the normal probability of residuals and the actual experimental value and predicted value for MRR. The experimental values are close to the predicted values with 95% CI. The residuals fall on the straight line in Fig. 1(a), showing the normal distribution of error.

The final equation for MRR in terms of coded factors:

$$\text{MRR (mm}^3/\text{min)} = 4.7151 + 0.4243 \times A - 0.4513 \times B$$
$$- 0.3007 \times C - 0.3721 \times B \times C$$
$$+ 0.7795 \times A^2 + 0.1919 \times B^2$$
$$+ 0.09289 \times C^2$$

$$\text{(Eq 7)}$$

The final equation for MRR in terms of actual factors:

$$\text{MRR (mm}^3/\text{min)} = 2821 - 46.0997 \times T_{ON} - 2.9188$$
$$\times T_{OFF} + 2.2603 \times SV - 0.0372$$
$$\times T_{OFF} \times SV + 0.1949 \times T_{ON}^2$$
$$+ 0.048 \times T_{OFF}^2 + 0.0037 \times SV^2$$

$$\text{(Eq 8)}$$

### 3.2 Effect of WEDM Parameters on Material Removal Rate

Figure 1(c), (d), (e), and (f) represents the effect of significant parameters such as $T_{ON}$, $T_{OFF}$, SV, and interaction of SV and $T_{OFF}$ on MRR. As can be seen in Fig. 1(c), MRR shows the increasing trend with $T_{ON}$. This is due to the fact that at a higher $T_{ON}$, the spark energy significantly increases which generates more heat to melt the material. In WEDM process, the energy needed to remove the material is achieved from the spark energy. So, the required thermal energy depends on the level of spark energy per pulse which finally converted into heat. The discharge energy is given by Eq 9 (Ref 5):

$$\text{Discharge energy} = \text{Discharge voltage} \times \text{Discharge current}$$
$$\times \text{Discharge duration}$$

$$\text{(Eq 9)}$$

As discharge voltage is almost constant, discharge duration and discharge current mainly influence the heating capability of individual spark. In case of zero ignition delay, the discharge duration becomes equal to pulse duration (i.e., $T_{ON}$). Discharge energy is directly influenced by $T_{ON}$. So, at higher $T_{ON}$, MRR increases due to substantial increase in the discharge energy.

Figure 1(d) shows the variation of MRR with $T_{OFF}$. The increase in MRR with the decrease in $T_{OFF}$ can be observed from experimental results. It was observed that spark's energy and intensity of spark decreased at higher $T_{OFF}$ which results in less removal of material from the workpiece, which finally led to lower MRR (Ref 3, 5). Simultaneously, with the increase in $T_{OFF}$, sparks frequency decreases which also reduced the MRR. The spark frequency can be given as Eq 10 (Ref 5):

$$\text{Sparks frequency (kHz)} = \frac{10^3}{T_{ON} + T_{OFF}} \qquad \text{(Eq 10)}$$

Figure 1(e) illustrates the effect of SV on MRR. The increase in SV has the inverse effect on MRR. This is due to the fact that the spark gap is widened at higher SV, which led to decrease sparking frequency (as given in Eq 10) and hence MRR finally decreased. Figure 1(f) displays the 3D response plot for MRR in terms of SV and $T_{OFF}$. It was noticed from the response plot that MRR is decreased by increasing $T_{OFF}$ from 54 to 58 μs and parallel increasing SV from 40 to 50 V. Similar effect of $T_{ON}$, $T_{OFF}$, and SV on MRR was also supported by Narendranath el al. (Ref 25) and Manjaiah et al. (Ref 26) findings for Ti$_{50}$Ni$_{42.4}$Cu$_{7.6}$ SMA and equiatomic NiTi SMA, respectively, in WEDM.

### 3.3 ANOVA for Surface Roughness

ANOVA results for $R_a$ are tabularized in Table 4; the F value of the model is 35.50 which suggests the significance of the developed model. The parameters $T_{ON}$, $T_{OFF}$, SV, interaction of $T_{ON}$ and SV, and square of $T_{ON}$ are the significant model terms having a $p$ value < 0.05 at 95% CI. It is observed that $T_{OFF}$ has the highest percentage contribution followed by $T_{ON}$ and SV for $R_a$. The probability value ($p$ value) for lack of fit is 0.4658 infers that the lack of fit is not significant relative to the pure error. The $R^2$ for the model is 0.9607 shows the closeness of predicted values and actual experimental values. The predicted
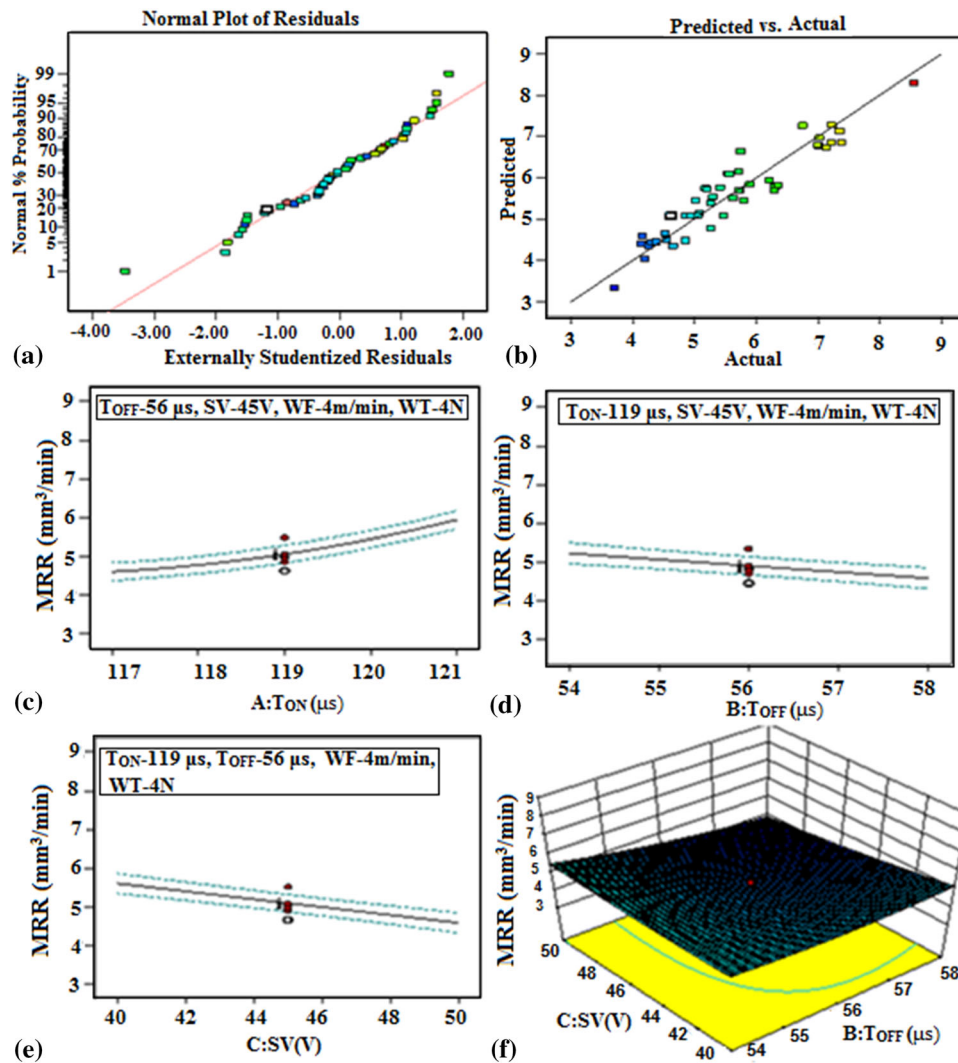
**Fig. 1** Residual graphs for MRR (a) normal probability vs. residuals, (b) actual experimental value vs. predicted value and effect of variable parameters, (c) TON, (d) $T_{OFF}$, (e) SV, (f) interaction of SV and $T_{OFF}$ on MRR

**Table 4  ANOVA table for surface roughness**

| Source | SS | DOF | MS | F value | p value Prob > F | Remarks | Percentage contribution |
|---|---|---|---|---|---|---|---|
| Model | 1.76 | 20 | 0.088 | 35.50 | < 0.0001 | Significant | … |
| A | 0.43 | 1 | 0.43 | 173.80 | < 0.0001 | Significant | 24.33 |
| B | 0.92 | 1 | 0.92 | 369.37 | < 0.0001 | Significant | 52.06 |
| C | 0.15 | 1 | 0.15 | 60.57 | < 0.0001 | Significant | 8.49 |
| AC | 0.13 | 1 | 0.13 | 50.96 | < 0.0001 | Significant | 7.36 |
| $A^2$ | 0.065 | 1 | 0.065 | 26.23 | < 0.0001 | Significant | 3.68 |
| Residual | 0.072 | 29 | 0.0024 | | | | |
| Lack of fit | 0.056 | 22 | 0.0025 | 1.13 | 0.4658 | Not significant | |
| Pure error | 0.016 | 7 | 0.0022 | | | | $R^2$ = 0.9607 |
| Corrected total | 1.767 | 49 | | | | | Adjusted-$R^2$ = 0.9337 |
| | | | | | | | Predicted $R^2$ = 0.8749 |
| | | | | | | | Adequate precision = 24.605 |

$R^2$ (0.8749) is in realistic agreement with the adjusted $R^2$ (0.9337). For $R_a$, adequate precision is 24.605 which designates the adequate model discrimination. The developed mathemat-

ical equation for surface roughness in coded parameters and actual parameters is given in Eq 11 and 12, respectively. The normal probability of residual graph and the actual experimen-

tal value and predicted value graph for $R_a$ are given in Fig. 2(a) and (b), respectively. The predicted values and experimental values at 95% CI are close as shown in Fig. 2(b).

The final equation for $R_a$ in terms of coded factors:

$$R_a\ (\mu m) = 2.07 + 0.1038 \times A - 0.1513 \times B - 0.0613 \times C + 0.0628 \times AC - 0.0451 \times A^2$$

$$\text{(Eq 11)}$$

The final equation in terms of actual factors:

$$R_a\ (\mu m) = -129.949 + 2.4248 \times T_{ON} + 0.1909 \times T_{OFF} - 0.7857 \times SV + 0.0063 \times T_{ON} \times SV - 0.0113 \times T_{ON}^2$$

$$\text{(Eq 12)}$$

### 3.4 Effect of WEDM Parameters on Surface Roughness

Figure 2(c), (d), (e) and (f) represents the effect of significant parameters, namely $T_{ON}$, $T_{OFF}$, SV, and interaction of SV and $T_{ON}$ on surface roughness. Figure 2(c) displays the effect of $T_{ON}$ on $R_a$. $R_a$ was found to increase with an increase in $T_{ON}$. In WEDM, at a higher value of $T_{ON}$, discharge energy [given in Eq 9] is increased. At higher discharge energy, more heat is available to remove the material and hence deeper and wider craters are formed at the machined surface. Finally, SR increases due to the formation of the deeper craters at the machined surface at higher $T_{ON}$.

The effect of $T_{OFF}$ on $R_a$ is shown in Fig. 2(d). $R_a$ shows the reverse trend with $T_{OFF}$. $R_a$ decreases with an increase in $T_{OFF}$. This is because of an increase in flushing time (time to wipe out the molten droplets on the machined surface) at higher $T_{OFF}$ (Ref 24). Simultaneously, as $T_{OFF}$ increases, sparking frequency decreases, and sparking-ampere increases. So, it is suggested that low sparking frequency is used for rough cutting operation, whereas high sparking frequency is preferred for the finishing operation.

Similar to $T_{OFF}$, the increase in SV has the inverse effect on $R_a$. Figure 2(e) shows the decreasing trend of $R_a$ with SV. This is due to the reason that at higher SV spark gap widened which led to decrease in sparking frequency and finally surface roughness decreases. Three-dimensional response plot for surface roughness in terms of SV and $T_{ON}$ is shown in Fig. 2(f). From the response plot, it can be seen that $R_a$ is increasing by increasing $T_{ON}$ from 117 to 121 μs and parallel decreasing SV from 40 to 50 V. Sharma et al. (Ref 27) and
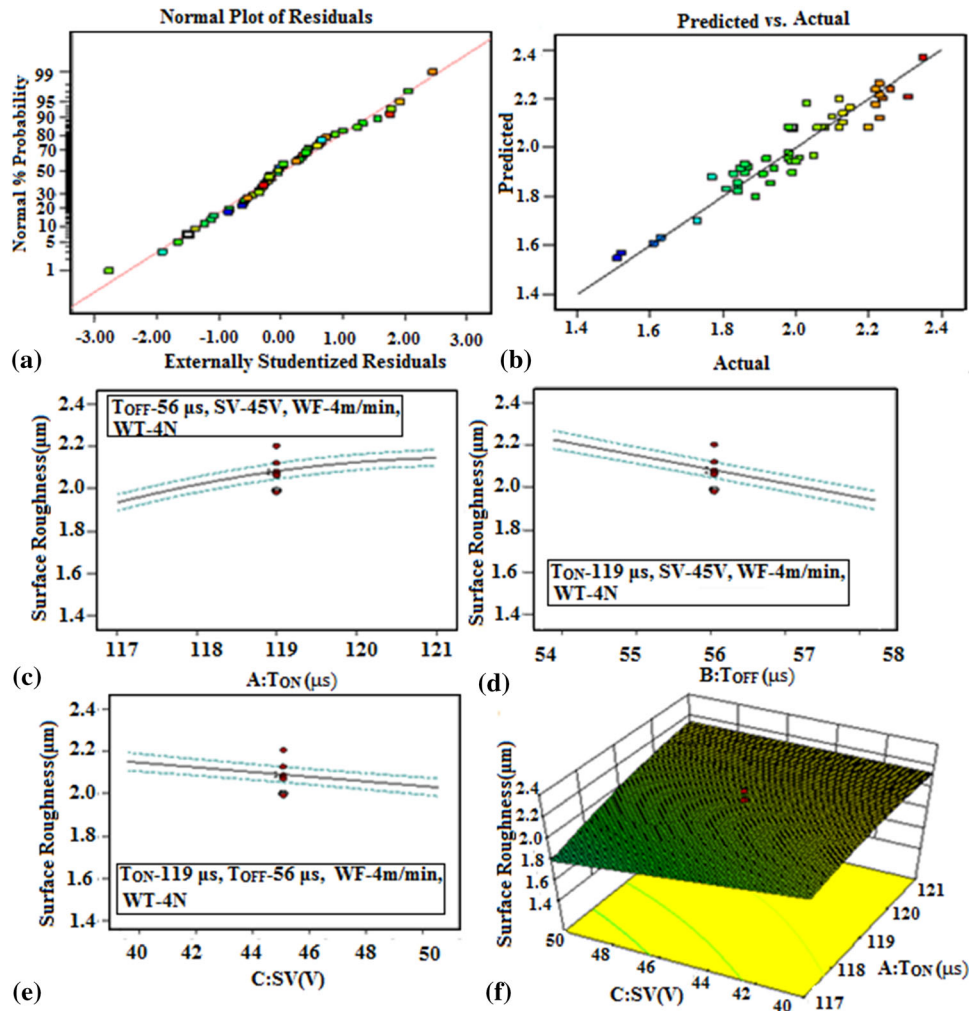


**Fig. 2** Residual graphs for surface roughness **a** normal probability vs. residuals, **b** actual experimental value vs. predicted value and effect of variable parameters, **c** TON, **d** $T_{OFF}$, **e** SV, **f** interaction of SV and TON on surface roughness

Manjaiah et al. (Ref 28) also encountered with similar findings for $R_a$ during WEDM of $Ni_{40}Ti_{60}$ SMA and NiTiCu SMA, respectively.

## 4. Multi-objective Optimization

### 4.1 Grey Relational Analysis (GRA) Technique

Among multi-response optimization technique, GRA technique can be utilized for solving the complex interrelationship. In GRA technique, multi-response optimization problem can be converted into single relational grade. GRA technique has been utilized to optimize MRR and $R_a$ for $Ni_{55.95}Ti4_{.05}$ SMA. In the multi-optimization using GRA, the following steps are involved (Ref 29):

**Step 1** Data preprocessing (Normalization of experimental data).

In GRA, first experimental results data are linearly normalized in the range from 0 to 1 which is known as grey relational generation. The experimental data can be normalized by three different approaches according to objective, i.e., "smaller the better," "larger the better" and "nominal the better." The expression for normalizing the data using smaller the better and larger the better type characteristics is given Eq 13 and 14:

For larger the better type objective (e.g., MRR)

$$z_i * (k) = \frac{\left[z_i^0(k) - \min\{z_i^0(k)\}\right]}{\left[\max\{z_i^0(k)\} - \min\{z_i^0(k)\}\right]} \qquad \text{(Eq 13)}$$

For smaller the better type objective (e.g., $R_a$)

$$z_i * (k) = \frac{\left[\max\{z_i^0(k)\} - z_i^0(k)\right]}{\left[\max\{z_i^0(k)\} - \min\{z_i^0(k)\}\right]} \qquad \text{(Eq 14)}$$

where $z_i^0(k)$ and $z_i*(k)$ are the original sequence and sequence after the data processing, respectively, whereas $\max z_i^0(k)$ is the largest value of $z_i^0(k)$ and $\min z_i^0(k)$ is the smallest value of $z_i^0(k)$.

**Step 2** Grey relation coefficient (GRC)

GRC represents the correlation between actual and desired experimental data. GRC is calculated as per Eq 15:

$$\beta_{0,i}(k) = \frac{[\Delta_{min} + \zeta\Delta_{max}]}{[\Delta_{oi}^*(k) + \zeta\Delta_{max}]} \quad 0 < \beta_{0,i}(k) \le 1 \qquad \text{(Eq 15)}$$

where $\beta_{0,i}(k)$ is grey relational coefficient, $\zeta$ is identification coefficients, $\zeta \in [0, 1]$ and generally 0.5 is used. $\Delta_{oi}(k)$ is the difference of the absolute value $z_0*(k)$ and $z_i*(k)$, i.e., $\Delta_{oi}(k) = |z_0*(k) - z_i*(k)|$, $\Delta_{min} = \min(\min \Delta_{oi}(k))$ and $\Delta_{max} = \max(\max \Delta_{oi}(k))$

**Step 3** Grey relational grade (GRG)

GRG is used for overall evaluation of multi-response characteristics. The average of GRC value is considered as GRG. GRG is given in Eq 16.

$$\Upsilon_i = \frac{1}{m}\sum_{k=1}^{m}\beta_{0,i}(k) \qquad \text{(Eq 16)}$$

where $m$ is the number of process response and the higher value of GRG signifies the closeness of parameters to the optimum solution. The higher value of GRG signifies the closeness of the corresponding set of parameters to the optimal.

The normalized value, deviation, GRC, and GRG values for individual experiment runs are given in Table 5. Experimental run 34 has the highest GRG (1) representing the best combination among 50 experimental runs. At experimental run 34, i.e., A (123 μs), B (56 μs), C (45 V), D (4 N), E (4 m/min), the max MRR (8.554 mm³/min) and min $R_a$ (2.12 μm) were achieved among 50 experiments. The mean response for overall GRG is given in Table 6. It was observed that $T_{ON}$, $T_{OFF}$, and SV were the significant parameters having the highest delta (max GRG–min GRG), whereas WF and WT are insignificant parameters for the improvement in GRG. This finding also validates the results of ANOVA for MRR and $R_a$. From Table 6, it can be observed that at $A_2B_1C_1D_{-1}E_1$ parameter setting, i.e., A (123 μs), B (58 μs), C (50 V), D (3 N), and E (5 m/min), respectively, max MRR and min $R_a$ can be achieved. $A_2B_1C_1D_{-1}E_1$ parameter setting is overall optimized level of input parameters suggested by GRA technique.

### 4.2 Confirmatory Experiment

Table 7 shows the optimized values obtained from confirmatory tests. The max MRR was 8.223 mm³/min and min $R_a$ was 1.93 μm obtained experimentally at optimized levels of parameters, whereas the value predicted by RSM model (Eq 8, 12) for MRR and $R_a$ was 7.842 mm³/min and 2.01 μm, respectively. The percentage error between the predicted and experimental value for both MRR and $R_a$ lies < 5% which endorses the accuracy of developed RSM model. With respect to initial setting ($A_{-1}B_{-1}C_{-1}D_{-1}E_{-1}$), an increment of 21.73% and decrement of 9.34% for MRR and $R_a$, respectively, were observed at optimal levels of parameters.

## 5. Surface Integrity Aspects

The processing and end use of the machined component are directly affected by surface characteristics of the machined part. During WEDM process, surface characteristics of the machined part are altered. In surface integrity aspects, the altered surface characteristics which affect the properties of workpiece material are measured (Ref 30). Surface integrity may be defined as the enhanced condition of the surface manufactured by any machining process or other processes related to surface generation. Surface integrity includes not only the topological (geometrical) aspects of the machined surface but also the physical, chemical, metallurgical, mechanical and biological aspect (Ref 31).

After getting the optimized parameters setting ($A_2B_1C_1D_{-1}E_1$), the surface integrity aspects such as surface morphology, surface topography, recast layer thickness, phase analysis, and micro-hardness analysis have been carried out at optimized parameter setting.

### 5.1 Surface Characteristics

Figure 3(a) and (b) illustrates the surface morphology and three-dimensional (3D) surface topography of the machined surface for $Ni_{55.95}Ti_{44.05}$ SMA at optimized parameters setting

**Table 5  Grey relational coefficient and grey relational grade for MRR and $R_a$**

| Std. run | Normal (MRR) | Normal ($R_a$) | Deviation (MRR) | Deviation ($R_a$) | GRC (MRR) | GRC ($R_a$) | GRG | Rank |
|---|---|---|---|---|---|---|---|---|
| 1 | 0.587 | 0.262 | 0.413 | 0.738 | 0.548 | 0.404 | 0.476 | 29 |
| 2 | 0.649 | 0.202 | 0.351 | 0.798 | 0.588 | 0.385 | 0.486 | 26 |
| 3 | 0.485 | 0.607 | 0.515 | 0.393 | 0.492 | 0.560 | 0.526 | 16 |
| 4 | 0.629 | 0.583 | 0.371 | 0.417 | 0.574 | 0.545 | 0.560 | 9 |
| 5 | 0.556 | 0.524 | 0.444 | 0.476 | 0.530 | 0.512 | 0.521 | 19 |
| 6 | 0.649 | 0.155 | 0.351 | 0.845 | 0.587 | 0.372 | 0.480 | 27 |
| 7 | 0.312 | 0.881 | 0.688 | 0.119 | 0.421 | 0.808 | 0.614 | 4 |
| 8 | 0.307 | 0.512 | 0.693 | 0.488 | 0.419 | 0.506 | 0.463 | 32 |
| 9 | 0.558 | 0.298 | 0.442 | 0.702 | 0.531 | 0.416 | 0.473 | 30 |
| 10 | 0.640 | 0.131 | 0.360 | 0.869 | 0.581 | 0.365 | 0.473 | 31 |
| 11 | 0.478 | 0.607 | 0.522 | 0.393 | 0.489 | 0.560 | 0.525 | 18 |
| 12 | 0.624 | 0.571 | 0.376 | 0.429 | 0.571 | 0.538 | 0.555 | 12 |
| 13 | 0.610 | 0.595 | 0.390 | 0.405 | 0.562 | 0.553 | 0.557 | 10 |
| 14 | 0.724 | 0.143 | 0.276 | 0.857 | 0.645 | 0.368 | 0.507 | 22 |
| 15 | 0.126 | 0.857 | 0.874 | 0.143 | 0.364 | 0.778 | 0.571 | 8 |
| 16 | 0.226 | 0.440 | 0.774 | 0.560 | 0.392 | 0.472 | 0.432 | 38 |
| 17 | 0.479 | 0.262 | 0.521 | 0.738 | 0.490 | 0.404 | 0.447 | 35 |
| 18 | 0.789 | 0.143 | 0.211 | 0.857 | 0.703 | 0.368 | 0.536 | 13 |
| 19 | 0.482 | 0.607 | 0.518 | 0.393 | 0.491 | 0.560 | 0.526 | 17 |
| 20 | 0.711 | 0.583 | 0.289 | 0.417 | 0.634 | 0.545 | 0.589 | 7 |
| 21 | 0.448 | 0.643 | 0.552 | 0.357 | 0.475 | 0.583 | 0.529 | 14 |
| 22 | 0.716 | 0.155 | 0.284 | 0.845 | 0.638 | 0.372 | 0.505 | 23 |
| 23 | 0.224 | 1.000 | 0.776 | 0.000 | 0.392 | 1.000 | 0.696 | 2 |
| 24 | 0.283 | 0.619 | 0.717 | 0.381 | 0.411 | 0.568 | 0.489 | 25 |
| 25 | 0.348 | 0.238 | 0.652 | 0.762 | 0.434 | 0.396 | 0.415 | 40 |
| 26 | 0.740 | 0.107 | 0.260 | 0.893 | 0.658 | 0.359 | 0.508 | 21 |
| 27 | 0.365 | 0.690 | 0.635 | 0.310 | 0.441 | 0.618 | 0.529 | 15 |
| 28 | 0.722 | 0.440 | 0.278 | 0.560 | 0.642 | 0.472 | 0.557 | 11 |
| 29 | 0.535 | 0.500 | 0.465 | 0.500 | 0.518 | 0.500 | 0.509 | 20 |
| 30 | 0.854 | 0.274 | 0.146 | 0.726 | 0.774 | 0.408 | 0.591 | 6 |
| 31 | 0.107 | 0.988 | 0.893 | 0.012 | 0.359 | 0.977 | 0.668 | 3 |
| 32 | 0.482 | 0.488 | 0.518 | 0.512 | 0.491 | 0.494 | 0.493 | 24 |
| 33 | 0.575 | 0.738 | 0.425 | 0.262 | 0.540 | 0.656 | 0.598 | 5 |
| 34 | 1.000 | 0.274 | 0.000 | 0.726 | 1.000 | 0.408 | 0.704 | **1** |
| 35 | 0.453 | 0.000 | 0.547 | 1.000 | 0.478 | 0.333 | 0.405 | 42 |
| 36 | 0.044 | 0.679 | 0.956 | 0.321 | 0.343 | 0.609 | 0.476 | 28 |
| 37 | 0.315 | 0.167 | 0.685 | 0.833 | 0.422 | 0.375 | 0.399 | 45 |
| 38 | 0.000 | 0.405 | 1.000 | 0.595 | 0.333 | 0.457 | 0.395 | 47 |
| 39 | 0.350 | 0.429 | 0.650 | 0.571 | 0.435 | 0.467 | 0.451 | 34 |
| 40 | 0.325 | 0.429 | 0.675 | 0.571 | 0.426 | 0.467 | 0.446 | 36 |
| 41 | 0.358 | 0.357 | 0.642 | 0.643 | 0.438 | 0.438 | 0.438 | 37 |
| 42 | 0.364 | 0.417 | 0.636 | 0.583 | 0.440 | 0.462 | 0.451 | 33 |
| 43 | 0.098 | 0.429 | 0.902 | 0.571 | 0.357 | 0.467 | 0.412 | 41 |
| 44 | 0.183 | 0.274 | 0.817 | 0.726 | 0.380 | 0.408 | 0.394 | 48 |
| 45 | 0.141 | 0.440 | 0.859 | 0.560 | 0.368 | 0.472 | 0.420 | 39 |
| 46 | 0.108 | 0.321 | 0.892 | 0.679 | 0.359 | 0.424 | 0.392 | 49 |
| 47 | 0.065 | 0.333 | 0.935 | 0.667 | 0.348 | 0.429 | 0.388 | 50 |
| 48 | 0.134 | 0.321 | 0.866 | 0.679 | 0.366 | 0.424 | 0.395 | 46 |
| 49 | 0.151 | 0.333 | 0.849 | 0.667 | 0.371 | 0.429 | 0.400 | 44 |
| 50 | 0.170 | 0.345 | 0.830 | 0.655 | 0.376 | 0.433 | 0.405 | 43 |

$(A_2B_1C_1D_{-1}E_1)$, respectively. From the SEM micrograph shown in Fig. 3(a), the presence of many pockmarks, spherical nodules, micro-voids, craters, drops of molten material, and micro-cracks on the machined surface can be distinctly observed. In WEDM process, the successive electrical sparks led to a transfer of intense heat into the machined surface result in the generation of discharge craters. The size of craters decides the quality of the machined surface (Ref 32). During $T_{OFF}$, some of the molten material was wiped out by the deionized water. However, the melted material remains left

resolidified on the machined surface to form lumps of debris. Pockmarks are formed on the machined surface due to entrap gases escaping from the redeposited material. The high temperature gradient experienced by outer machined surface results in the existence of thermal and tensile stresses; as a result, the micro-cracks were formed on the machined component.

Figure 3(b) depicts the three-dimensional surface topography which describes the height of protrusion and depth of depression on the machined surface at optimized parameters

setting ($A_2B_1C_1D_{-1}E_1$). In Fig. 3(b), it can be clearly seen that the depth of material removed from the machined surface was approximately 60 μm. In WEDM process, after the removal of material, a crater is formed on the machined due to sparking phenomenon. So, the crater depth is approximately 60 μm.

### 5.2 Recast Layer Thickness

Figure 4(a) and (b) illustrates the recast layer deposited on the machined surface and elemental composition of the recast layer using EDS at optimized parameters setting ($A_2B_1C_1D_{-1}E_1$). A recast layer of thickness 19.51 μm is formed on the machined surface which is inspected by the cross-sectional view of the machined surface through SEM. The elemental composition of the machined surface using EDS reveals the existence of foreign elements such as copper (Cu), zinc (Zn), carbon (C), and oxygen (O) from the dielectric and wire electrode. In EDS of machined surface, 4.15% Cu, 0.33% Zn, 2.19% O, and 14.48% C as foreign elements were detected. Apart from the base material (Ni and Ti), the existence of the foreign elements in the recast layer is because of chemical reaction at the elevated temperature. At higher temperature, the foreign elements were diffused to the machined surface.

### 5.3 XRD Analysis

The XRD peaks for $Ni_{55.95}Ti_{44.05}$ SMA's machined surface at optimized parameters setting ($A_2B_1C_1D_{-1}E_1$) with the detailed information are illustrated in Fig. 5. The identified peaks of XRD divulge the formation of oxides and compounds of Ni, Ti, Zn and Cu, namely NiTi, $Ni_4Ti_3$, $Ti_4O_3$, $Cu_5Zn_8$, $Ni(TiO_3)$, and NiZn on the machined surface. The oxides and compounds of Ni and Ti were formed because of the high reactivity of Ti and Ni atoms. The presence of compounds of Cu and Zn is due to the diffusion of foreign atoms from brass wire and dielectric fluid to the machined surface. The shifting of peaks toward the right side in the XRD pattern indicates the presence of tensile residual stress on machined surface. The results of XRD pattern also support the EDS results of the recast layer.

**Table 6  Response table for GRG**

| Level | $T_{ON}$ (A) | $T_{OFF}$ (B) | SV (C) | WF (D) | WT (E) |
|---|---|---|---|---|---|
| (− 2) | 0.5984 | 0.4054 | 0.3985 | 0.4507 | 0.4376 |
| (− 1) | 0.5364 | 0.5008 | 0.5113 | **0.5276** | 0.5136 |
| (0) | 0.4166 | 0.4428 | 0.4483 | 0.4419 | 0.4424 |
| (1) | 0.5139 | **0.5495** | **0.5389** | 0.5226 | **0.5366** |
| (2) | **0.7039** | 0.4760 | 0.3949 | 0.4461 | 0.4509 |
| Delta | 0.2873 | 0.14406 | 0.14404 | 0.0857 | 0.0990 |
| Rank | 1 | 2 | 3 | 5 | 4 |

Bold values indicate the corresponding parameters for optimization

### 5.4 Analysis of Micro-hardness

The variation of micro-hardness for the machined surface of $Ni_{55.95}Ti_{44.05}$ SMA at optimized parameters setting ($A_2B_1C_1D_{-1}E_1$) is displayed in Fig. 6. It was observed that the micro-hardness in the vicinity of the outer machined surface was increased approximately 1.98 times as compared to the bulk hardness of $Ni_{55.95}Ti_{44.05}$ SMA. This increase in hardness may be due to either oxides formation or quenching effect. In WEDM process, the outer surface is exposed to extremely high temperature and experiences sudden cooling by the pressurized dielectric, which can increase the hardness near the outer surface. The oxide formation ($NiTiO_3$ and $Ti_4O_3$) and the diffusion of another alloying element in the recast layer may
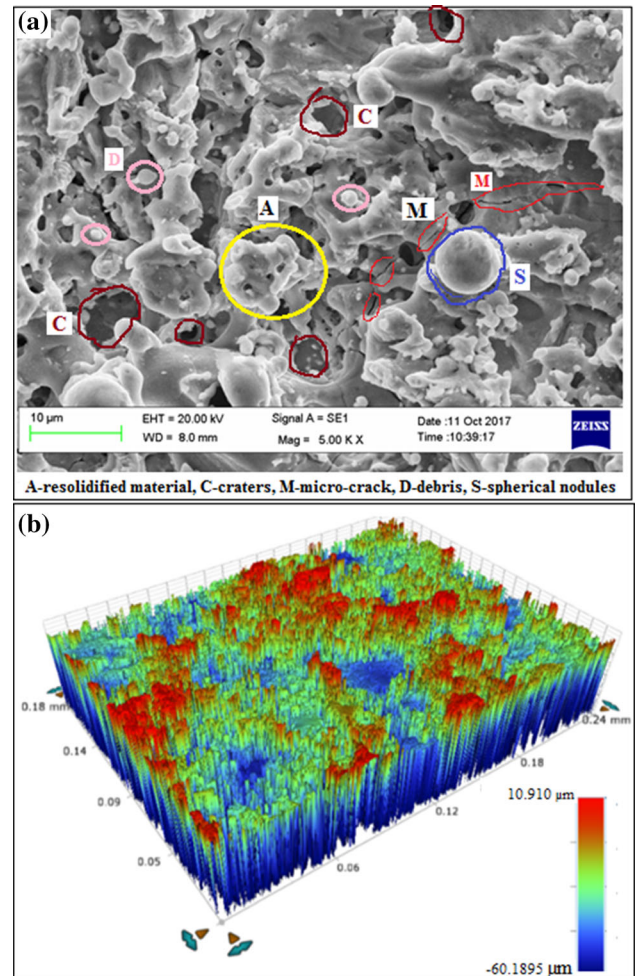


**Fig. 3** Surface characteristics **a** SEM micrograph and **b** 3D surface topography at optimal parameters setting (A2B1C1D-1E1)

**Table 7  Experimental validations of predicted value at optimal parameter level**

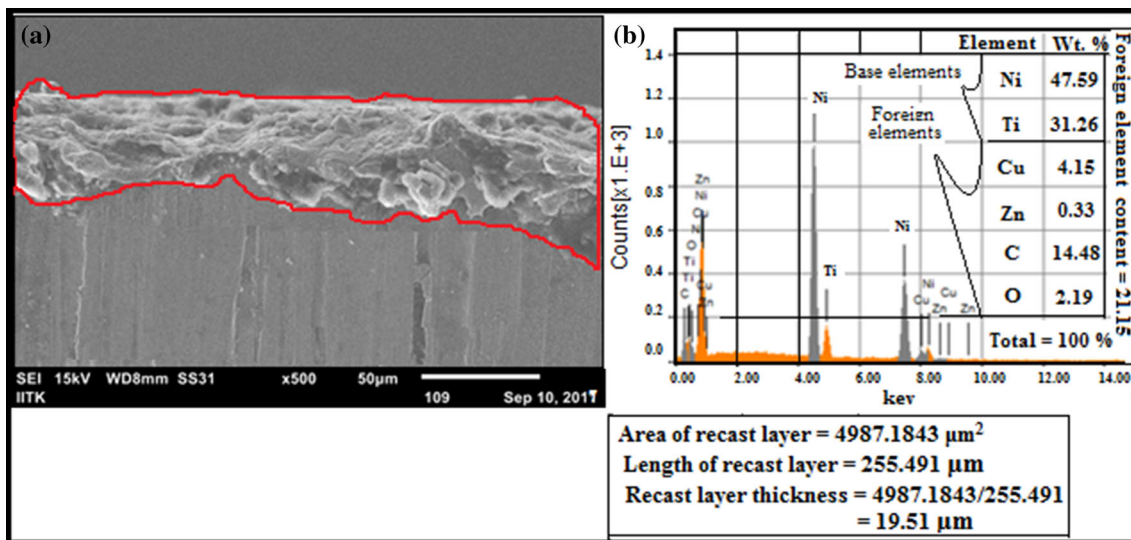| | | Optimal condition | | |
|---|---|---|---|---|
| | Initial setting | Predicted value | Experimental value | Error (Δ), % |
| Level | $A_{-1}B_{-1}C_{-1}D_{-1}E_{-1}$ | $A_2B_1C_1D_{-1}E_1$ | $A_2B_1C_1D_{-1}E_1$ | |
| MRR ($mm^3$/min) | 6.755 | 7.842 | 8.223 | 4.858 |
| $R_a$ (μm) | 2.13 | 2.01 | 1.93 | − 3.980 |

**Fig. 4** Cross-sectional SEM micrograph **a** recast layer formed on the machined surface and **b** EDS of recast layer at optimal parameters setting (A2B1C1D-1E1)
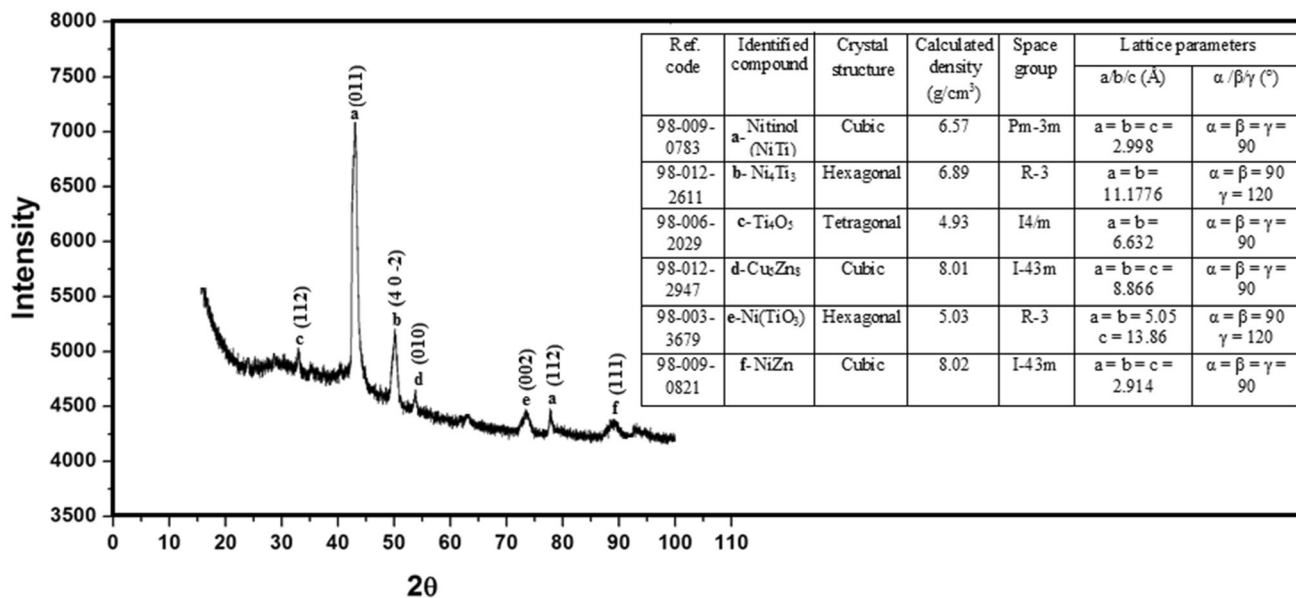


**Fig. 5** XRD peaks for machined surface at optimal parameters setting (A2B1C1D-1E1)

also be responsible for hardening effect. Similar hardening effect near the outer machined surface in WEDM process was also observed by Hsieh et al. (Ref 12) and Bisaria and Shandilya (Ref 5) for NiTi-Cr/Zr ternary SMA and Ni-rich SMA, respectively.

## 6. Conclusions

In this experimental work, MRR and surface roughness for $Ni_{55.95}Ti_{44.05}$ SMA have been mathematically modeled and analyzed using RSM technique. Surface integrity aspects at the optimized level of parameters were studied. Based on the experimental results and analysis, the following findings can be drawn.

1. As per GRA technique, WEDM optimized parameter setting for $Ni_{55.95}Ti_{44.05}$ SMA was $A_2B_1C_1D_{-1}E_1$, i.e., A ($T_{ON}$ = 123 µs), B ($T_{OFF}$ = 58 µs), C (SV = 50 V), D (WT = 3 N), and E (WF = 5 m/min). An increment of 21.73% for MRR and decrement of 9.34% for $R_a$ were achieved compared to initial setting $A_{-1}B_{-1}C_{-1}D_{-1}E_{-1}$, i.e., A ($T_{ON}$ = 117 µs), B ($T_{OFF}$ = 54 µs), C (SV = 40 V), D (WT = 3 N), and E (WF = 3 m/min). The percentage error between experimental and predicted value was obtained 4.858 and 3.980 for MRR and $R_a$, respectively, which validates the accuracy of the developed RSM model.

2. Micro-structural analysis of machined surface reveals that the machined surface contains micro-voids, micro-cracks, debris, and spherical nodules, whereas the 3D surface
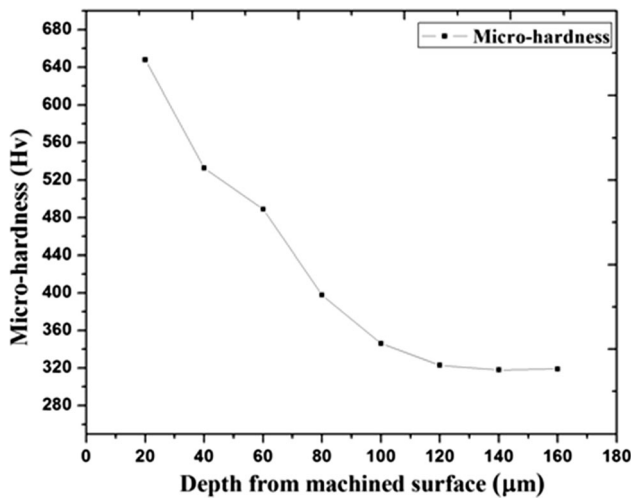
**Fig. 6** Micro-hardness variation with the depth from machined surface at optimal parameters setting (A2B1C1D-1E1)

topography shows the depth of crater was approximately 60 μm.

3. A recast layer of thickness 19.51 μm with 21.15% foreign elements (Cu, Zn, O, and C) from brass wire electrode and ionization of dielectric fluid transferred to the machine surface was formed.

4. XRD analysis of the machined surface exposes the presence of the compounds of Ni and Ti such as NiTi, $Ni_4Ti_3$, $Ti_4O_3$, $Cu_5Zn_8$, $Ni(TiO_3)$, and NiZn.

5. Micro-hardness near the machined surface was found to be increased 1.98 times as compared to bulk hardness because of quenching effect and oxide formation.

## References

1. J.M. Jani, M. Leary, A. Subic, and M.A. Gibson, A Review of Shape Memory Alloy Research, Applications and Opportunities, *Mater. Des.*, 2014, **56**, p 1078–1113

2. C. Velmurugan, V. Senthilkumar, S. Dinesh, and D. Arulkirubakaran, Machining of NiTi-Shape Memory Alloys—A Review, *Mach. Sci. Technol.*, 2017, **22**(3), p 355–401

3. H. Bisaria and P. Shandilya, Experimental Studies on Electrical Discharge Wire Cutting of Ni-Rich NiTi Shape Memory Alloy, *Mater. Manuf. Process.*, 2017, **33**(9), p 977–985

4. B. Ramachandran, C.H. Chen, P.C. Chang, Y.K. Kuo, C. Chen, and S.K. Wu, Thermal and Transport Properties of As-Grown Ni-Rich TiNi Shape Memory Alloys, *Intermetallics*, 2015, **60**, p 79–85

5. H. Bisaria and P. Shandilya, The Machining Characteristics and Surface Integrity of Ni-Rich NiTi Shape Memory Alloy Using Wire Electric Discharge Machining, *Proc. IMechE C J. Mech. Eng. Sci.*, 2018, https://doi.org/10.1177/0954406218763447

6. A. Rao, A.R. Srinivasa, and J.N. Reddy, *Introduction to Shape Memory Alloys, Design of Shape Memory Alloy (SMA) Actuators*, Springer, New York, 2015

7. P. Shandilya, H. Bisaria, and P.K. Jain, Parametric Study on Recast Layer During Electric Discharge Wire Cutting (EDWC) of Ni-Rich NiTi Shape Memory Alloy, *J. Micro Manuf.*, 2018, **1**(2), p 134–141

8. M. Manjaiah, S. Narendranath, and S. Basavarajappa, Review on Nonconventional Machining of Shape Memory Alloys, *Trans. Nonferr. Met. Soc.*, 2014, **24**, p 12–21

9. M. Karimzadeh, M.R. Aboutalebi, M.T. Salehi, S.M. Abbasi, and M. Morakabati, Adjustment of Aging Temperature for Reaching Superelasticity in Highly Ni-Rich Ti-51.5Ni NiTi Shape Memory Alloy, *Mater. Manuf. Process.*, 2016, **31**, p 1014–1021

10. K. Weinert, V. Petzoldt, and D. Kotter, Turning and Drilling of NiTi Shape Memory Alloys, *CIRP Ann. Manuf. Technol.*, 2004, **53**, p 65–68

11. Y. Guo, A. Klink, C. Fu, and J. Snyder, Machinability and Surface Integrity of Nitinol Shape Memory Alloy, *CIRP Ann. Manuf. Technol.*, 2013, **62**, p 83–86

12. S.F. Hsieh, S.L. Chen, H.C. Lin, M.H. Lin, and S.Y. Chiou, The Machining Characteristics and Shape Recovery Ability of Ti-Ni-X (X = Zr, Cr) Ternary Shape Memory Alloys Using the Wire Electrodischarge Machining, *Int. J. Mach. Tools Manuf.*, 2009, **49**, p 509–514

13. M.J. Haddad, F. Alihoseini, M. Hadi, M. Hadad, A.F. Tehrani, and A. Mohammadi, An Experimental Investigation of Cylindrical Wire Electrical Discharge Turning Process, *Int. J. Adv. Manuf. Technol.*, 2010, **46**, p 1119–1132

14. H. Bisaria and P. Shandilya, Experimental Investigation on Wire Electric Discharge Machining (WEDM) of Nimonic C-263 Superalloy, *Mater. Manuf. Process.*, 2019, **34**(1), p 83–92

15. K. Mouralova, J. Kovar, L. Klakurkova, and T. Prokes, Effect of Width of Kerf on Machining Accuracy and Subsurface Layer After WEDM, *J. Mater. Eng. Perform.*, 2018, **27**, p 1908. https://doi.org/10.1007/s11665-018-3239-4

16. A. Giridharan and G.L. Samuel, Analysis on the Effect of Discharge Energy on Machining Characteristics of Wire Electric Discharge Turning Process, *Proc. IMechE B J. Eng. Manuf.*, 2015, **230**(11), p 2064–2081

17. S. Bhattacharya, G.J. Abraham, A. Mishra, V. Kain, and G.K. Dey, Corrosion Behavior of Wire Electrical Discharge Machined Surfaces of P91 Steel, *J. Mater. Eng. Perform.*, 2018, **27**, p 4561. https://doi.org/10.1007/s11665-018-3558-5

18. M. Manjaiah, S. Narendranath, S. Basavarajappa, and V.N. Gaitonde, Effect of Electrode Material in Wire Electro Discharge Machining Characteristics of $Ti_{50}Ni_{50-x}Cu_x$ Shape Memory Alloy, *Precis. Eng.*, 2015, **41**, p 68–77

19. J.F. Liu, Y.B. Guo, T.M. Butler, and M.L. Weaver, Crystallography, Compositions, and Properties of White Layer by Wire Electrical Discharge Machining of Nitinol Shape Memory Alloy, *Mater. Des.*, 2016, **109**, p 1–9

20. G. Rajyalakshmi and P.V. Ramaiah, Multiple Process Parameter Optimization of Wire Electrical Discharge Machining on Inconel 825 Using Taguchi Grey Relational Analysis, *Int. J. Adv. Manuf. Technol.*, 2013, **69**, p 1249–1262

21. A. Saha and S.C. Mondal, Experimental Investigation and Modelling of WEDM Process for Machining Nano-structured Hardfacing Material, *J. Braz. Soc. Mech. Sci. Eng.*, 2017, **39**, p 3439–3455

22. H. Majumder, T.R. Paul, V. Dey, P. Dutta, and A. Saha, Use of PCA-Grey Analysis and RSM to Model Cutting Time and Surface Finish of Inconel 800 During Wire Electro Discharge Cutting, *Measurement*, 2017, **107**, p 19–30

23. D.C. Montgomery, *Design and Analysis of Experiments*, 4th ed., Wiley, New York, 2001

24. H. Bisaria and P. Shandilya, Study on Effect of Machining Parameters on Performance Characteristics of Ni-Rich NiTi Shape Memory Alloy During Wire Electric Discharge Machining, *Mater. Today Proc.*, 2018, **5**, p 3316–3324

25. S. Narendranath, M. Manjaiah, S. Basavarajappa, and V.N. Gaitonde, Experimental Investigations on Performance Characteristics in Wire Electro Discharge Machining of $Ti_{50}Ni_{42.4}Cu_{7.6}$ Shape Memory Alloy, *Proc. IMechE B J. Eng. Manuf.*, 2013, **227**(8), p 1180–1187

26. M. Manjaiah, S. Narendranath, S. Basavarajappa, and V.N. Gaitonde, Wire Electric Discharge Machining Characteristics of Titanium Nickel Shape Memory Alloy, *Trans. Nonferr. Met. Soc.*, 2014, **24**, p 3201–3209

27. N. Sharma, T. Raj, and K.K. Jangra, Parameter Optimization and Experimental Study on Wire Electrical Discharge Machining of Porous $Ni_{40}Ti_{60}$ Alloy, *Proc. IMechE B J. Eng. Manuf.*, 2015, **231**(6), p 956–970

28. M. Manjaiah, S. Narendranath, and S. Basavarajappa, Wire Electro Discharge Machining Performance of TiNiCu Shape Memory Alloy, *Silicon*, 2016, **8**, p 467–475

29. S. Datta, A. Bandyopadhyay, and P.K. Pal, Solving Multi-criteria Optimization Problem in Submerged Arc Welding Consuming a Mixture of Fresh Flux and Fused Slag, *Int. J. Adv. Manuf. Technol.*, 2008, **35**, p 935–942

30. D. Ulutan and T. Ozel, Machining Induced Surface Integrity in Titanium and Nickel Alloys: A Review, *Int. J. Mach. Tools Manuf.*, 2011, **51**, p 250–280

31. A. Thakur and S. Gangopadhyay, State-of-the-Art in Surface Integrity in Machining of Nickel-Based Super Alloys, *Int. J. Mach. Tools Manuf.*, 2016, **100**, p 25–54

32. H. Bisaria and P. Shandilya, Study on Crater Depth During Material Removal in WEDC of Ni-Rich Nickel–Titanium Shape Memory Alloy, *J Braz. Soc. Mech. Sci. Eng.*, 2019, **41**, p 157. https://doi.org/10.1007/s40430-019-1655-5